

High-Speed Probe Card Analysis Using Real-time Machine Vision and Image Restoration Technique

by

Bonghun Shin

A thesis

presented to the University of Waterloo

in fulfillment of the

thesis requirement for the degree of

Master of Applied Science

in

Mechanical Engineering

Waterloo, Ontario, Canada, 2013

© Bonghun Shin 2013

I hereby declare that I am the sole author of this thesis. This is a true copy of the thesis, including any required final revisions, as accepted by my examiners.

I understand that my thesis may be made electronically available to the public.

Abstract

There has been an increase in demand for the wafer-level test techniques that evaluates the functionality and performance of the wafer chips before packaging them, since the trend of integrated circuits are getting more sophisticated and smaller in size. Throughout the wafer-level test, the semiconductor manufacturers are able to avoid the unnecessary packing cost and to provide early feedback on the overall status of the chip fabrication process. A probe card is a module of wafer-level tester, and can detect the defects of the chip by evaluating the electric characteristics of the integrated circuits(IC's). A probe card analyzer is popularly utilized to detect such a potential probe card failure which leads to increase in the unnecessary manufacture expense in the packing process.

In this paper, a new probe card analysis strategy has been proposed. The main idea in conducting probe card analysis is to operate the vision-based inspection on-the-fly while the camera is continuously moving. In doing so, the position measurement from the encoder is firstly synchronized with the image data that is captured by a controlled trigger signal under the real-time setting. Because capturing images from a moving camera creates blurring in the image, a simple deblurring technique has been employed to restore the original still images from blurred ones. The main ideas are demonstrated using an experimental test bed and a commercial probe card. The experimental test bed has been designed that comprises a micro machine vision system and a real-time controller, the configuration of the low cost experimental test bed is proposed. Compared to the existing stop-and-go approach, the proposed technique can substantially enhance the inspection speed without additional cost for major hardware change.

Acknowledgements

I would like to thank my supervisor, Prof. Soo Jeon, for his support and guidance at every step of my graduate studies. Also, I would like to thank Dr. Hyock-Ju Kwon for his technical discussion and support as well as consulting with me about my career planning. Sincere thanks go out to my friends and colleagues at the office: Hyunki, Hyunsung, Jiwon, Tong, Kamal, and Vahid. Especially, I would like to thank my project colleague, Jiwon, who shared his idea with me and helped me facilitate my research. I would also like to thank Hyunki and Hyunsung who shared their idea and friendship. I would like to offer gratitude to my project colleagues at SDA Inc. and Sedicon: Chang-Min Im and Cheong-Su Han, for their cooperation to build the experiment.

Finally, I would like to thank my children: Chaehong, Chaelin, and Yule, for waiting for their father over the last two year. I would like to express my appreciation to my graceful wife, Jeongsoon, for her unconditional love, moral support, and understanding. I don't think I would have made this achievement without your love, support, and faith in me.

Table of Contents

List of Tables	viii
List of Figures	ix
1 Introduction	1
1.1 Motivation	1
1.2 Research Approach	4
2 Literature Review	6
2.1 Application	6
2.1.1 Wafer-level tester	7
2.1.2 Probe Card	7
2.1.3 Probe Card Analyzer	10
2.2 Real-time Coordination of Vision and Motion Data	12
2.2.1 Real-time System	13
2.2.2 Latency	14

2.3	Restoration of Image Blurred by Linear Motion	16
2.3.1	Introduction	16
2.3.2	Image formation	17
2.3.3	Linear motion blur	19
2.3.4	Image Restoration	20
3	Experimental Test Bed	24
3.1	Configuration of the Micro Machine Vision	25
3.1.1	Micro optic design	25
3.1.2	Stage and mount	30
3.2	Configuration of Real-time Controller	30
3.2.1	Configuration	30
3.2.2	Connection	31
4	Experimental Results	33
4.1	Experimental test condition	33
4.2	Verification of the image restoration	36
4.3	Verification of combined image	37
4.4	Verification of overall accuracy	39
5	Conclusion and Future Work	42
5.1	Conclusion	42
5.2	Future Work	43

List of Tables

2.1	Probe card technology by manufacturers [8]	9
3.1	Specification of the components of the micro machine vision	28
3.2	Spatial resolution of the vision image	29
3.3	Specification of the components of the x - y - z stage	31
4.1	Experimental test conditions.	36
4.2	Error verification of the combined image[Unit: μm]	38

List of Figures

1.1	A probe card and the analyzer, Cantilever type. (<i>SDA Technology Co., Ltd.</i>)	2
2.1	Schematic of the wafer-level test	8
2.2	Probe with contact pressure applied and resulting scrub [8]	9
2.3	Vertical and MEMS type of probe card. (<i>SDA Technology Co., Ltd.</i>) . . .	11
2.4	Image acquisition algorithm	12
2.5	Value function for soft and hard real-time [41]	14
2.6	Timing diagrams of vision events and the object position	14
2.7	Image formation model [4]	18
3.1	Overview of the tabletop probe analysis system used for experiment.	24
3.2	Configuration of the machine vision.	26
3.3	A sample still image of pin tips.	27
3.4	Spatial Resolution Calibration	29
3.5	Configuration of realtime controller.	32

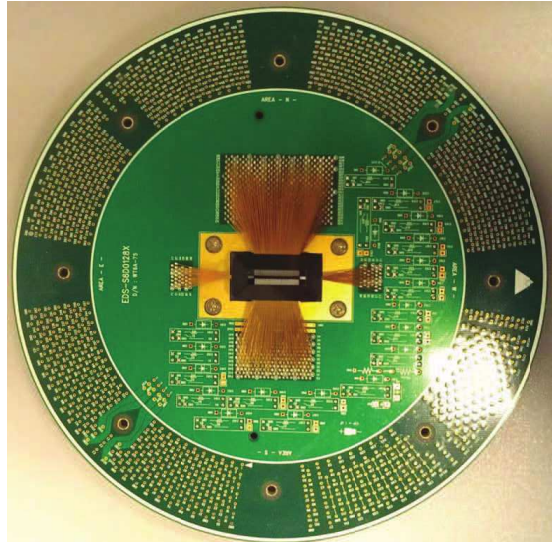
4.1	Real-time Image Processing Algorithm	34
4.2	Image overlapping for a cropped pin.	35
4.3	Comparison of sample images for three different cases.	37
4.4	Comparison between combined and reference still image	38
4.5	Mean and standard deviation of measurement errors of tip position and radius.	40
4.6	Histograms that show error distributions of x , y and r for two different speeds of camera movement.	41

Chapter 1

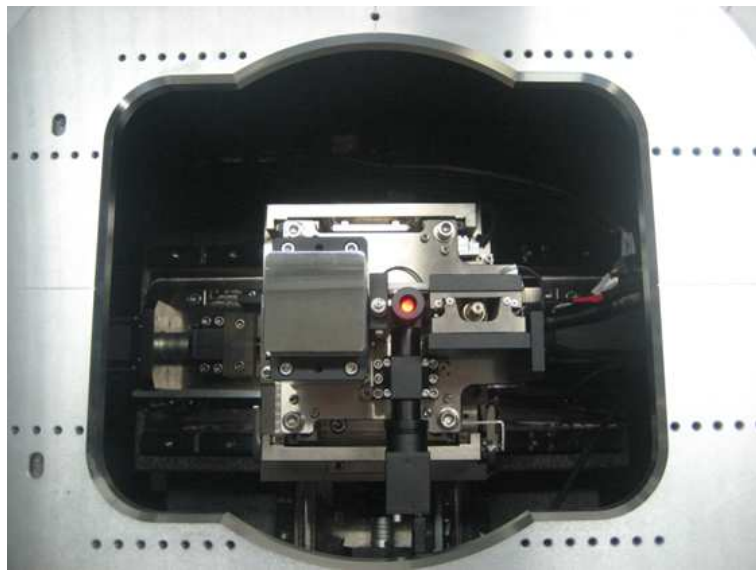
Introduction

1.1 Motivation

As integrated circuits (IC's) are getting more complex and smaller in size, a demand has been growing for the wafer-level test equipment to be capable of more sophisticated examination of device functionalities [29, 27]. One consequence of this recent trend is that the probe card, which provides a mechanical and electrical interface between the tester and the IC, has become more intricate [38] and increasingly dense with the number of probe pins easily going over several thousands [23, 34]. Figure 1.1(a) shows an example of existing probe cards. Electrical connection between the IC and the tester (i.e. the wafer prober) is made through wires branching out from the epoxy center ring. The cantilever pins are stacked around the center ring and make a physical contact with wafer dies. The magnified view of the cantilever type probe tips is shown in Fig. 2.3(a). The cantilever pin is one of three main types of probe cards widely used in industry. Two other types include the vertical type [23] and the MEMS (micro-electro-mechanical-system) type [38, 17, 18, 16].



(a) A probe card with cantilever pins.



(b) The main part of a probe card analyzer.

Figure 1.1: A probe card and the analyzer, Cantilever type. (*SDA Technology Co., Ltd.*)

During the probe card manufacturing, the card manufacturer needs to inspect it for a number of specifications on mechanical (alignment, planarity, tip radius, missing tips, etc.) as well as electrical (leakage, capacitance, etc.) properties. The test equipment used in this process is called the probe card analyzer. When IC manufacturers use probe cards, the probe pins get to wear and deteriorate as they are put in operation through repeated mechanical contacts with the IC pads. Hence, the IC manufacturers also need to equip them with the probe card analyzer to routinely monitor the status and integrity of the probe card in use. Figure 1.1(b) shows the main inspection module of a probe card analyzer (*SDA Technology Co. Ltd, Korea*). The probe card is placed on top of the module with the probe pins pointing downward so that the camera can take their images from below. The camera is mounted to the x - y stage and can be moved to different pin locations.

A major issue in conducting probe card analysis is that the inspection time increases in proportion to the number of pins. Thus, as a result of increased pin numbers, the test speed has become one of deciding factors in evaluating the performance of probe card analyzers. Among items to be inspected by a probe card analyzer, there are two mechanical properties that are essential and time-consuming: the planar alignment (x and y coordinates) and the tip diameter of each probe pin. As is done in typical machine vision applications [40], such mechanical properties are often optically (thus non-contact) inspected using the digital imaging system of the probe card analyzer where the stop-and-go strategy is taken to inspect one pin at a time. The target point for the stage to be positioned for each pin is provided by the predefined location map of probe pins. For each pin to be inspected, the stage needs to come to a complete stop before an image is taken and analyzed. In this way, the speed of 1 probe tip per second will result in the total inspection time close to three hours for a 10,000-pin probe card. Recently, there have been some attempts to use

other non-contact metrology techniques such as stereo vision and laser scanning [24], but they are still limited by performance and the cost for setting up the system.

1.2 Research Approach

This paper proposes a simple and cost-effective way to increase the inspection speed for the above mentioned inspection tasks. The basic idea is to capture the vision image and to process it on-the-fly while the camera is moving. Despite its simplicity, there are two major issues for this approach to be implemented in precision applications: (non-real-time) latency and image blurring. Since the vision and the stage may run asynchronously at different sample rates, it is a challenge to figure out at what location the stage was located while the image is being captured. Furthermore, the movement during the camera exposure causes imperfect image formation or blurring. To address these issues, we adopt deterministic sampling for machine vision and image restoration technique. Firstly, vision images have been sampled in a time-critical way using a real-time trigger such that the visual sensing is synchronized with the position measurement. With some simple calibration of event timings based on stage motion data, we can establish a consistent latency to coordinate the timing of position data with that of the vision image. Such a hard real-time image capturing technique has also been used in some of recent motion control and tracking applications [36, 11]. Secondly, to recover the clear vision data from the imperfect image, the advanced image restoration techniques or deblurring [2, 4, 26, 9] has been employed. The deblurring technique has long been used in various industrial applications, yet its use in micro-scale inspection is still rare [2]. The image of a moving object can also be acquired with little blurring if we use a high speed camera and a high power strobed illumination but it may greatly increase the implementation cost.

The remainder of this paper is organized as follows. The literature review is explained in Chapter 2 which explains the application background and the major technical issues such as the real-time machine vision and the image restoration techniques. Chapter 3 describes the overview of experimental test bed along with its main specifications, which has been designed to prove the main concept of the probe card analysis strategy proposed in this paper. An example probe card is then inspected using the test bed and the results are presented in Chapter 4. Finally, we summarize the results and propose the future work in Chapter 5.

Chapter 2

Literature Review

In this chapter, background research performed on the proposed probe card analysis are provided. Firstly, the probe card analyzer which include wafer-level tester, probe cards, and probe card analyzers are introduced. Afterwards, the major technical issues of the proposed high-speed real-time machine vision applications are reviewed. Technical background on the basic approach taken are also provided.

2.1 Application

This section offers background information regarding the inspection process of an integrated circuits fabrication and inspection module and inspection devices. Firstly, wafer-level tester that finds the defective chips before packing process is introduced. Secondly, several types of probe card are introduced. Finally, probe card analyzer that is the research topic of this paper is introduced.

2.1.1 Wafer-level tester

The wafer-level test, often referred to as probe test, is the core process of the probe station of the semiconductor equipment which test the functionality and performance of semiconductor after the wafer bumping process. By selecting and rejecting defective chips at the early stage, the manufacturer will reduce the unnecessary packing cost. Moreover, wafer-level test data offers early feedback on the overall status of the chip fabrication process [20]. Figure 2.1 shows the wafer-level test system which consists of a main frame, a wafer prober, and a probe card. The main frame is an analyzer which send electric signals and analyze the electric characteristics of the IC. The wafer prober comprises a wafer chuck, linear stages, and a test head which includes a tester, performance boards, and a probe card. The tester of the wafer prober is a measurement device which obtains electric characteristics when the probe tip and each bump in the wafer comes become connected through physical contact. The probe card is a module where device defects are found by the input/output of electric signal through the interface between the tester and the IC. The probe tip in the probe card makes contact with each bump in the wafer for the measurement of the electric characteristics of the IC.

2.1.2 Probe Card

The most common type of probe cards is the cantilever probe card which uses an array of horizontal needles to establish electrical contact with bumps on the wafer. A magnified and cross section view of a cantilever probe card is illustrated in Fig. 2.3(a). Since cantilever probe cards using horizontal needles are usually application-specific, the cantilever probe cards have many benefits and are highly utilized in wafer-level tests. However, due to some of the inherent physical limitation, it is becoming more difficult to use cantilever

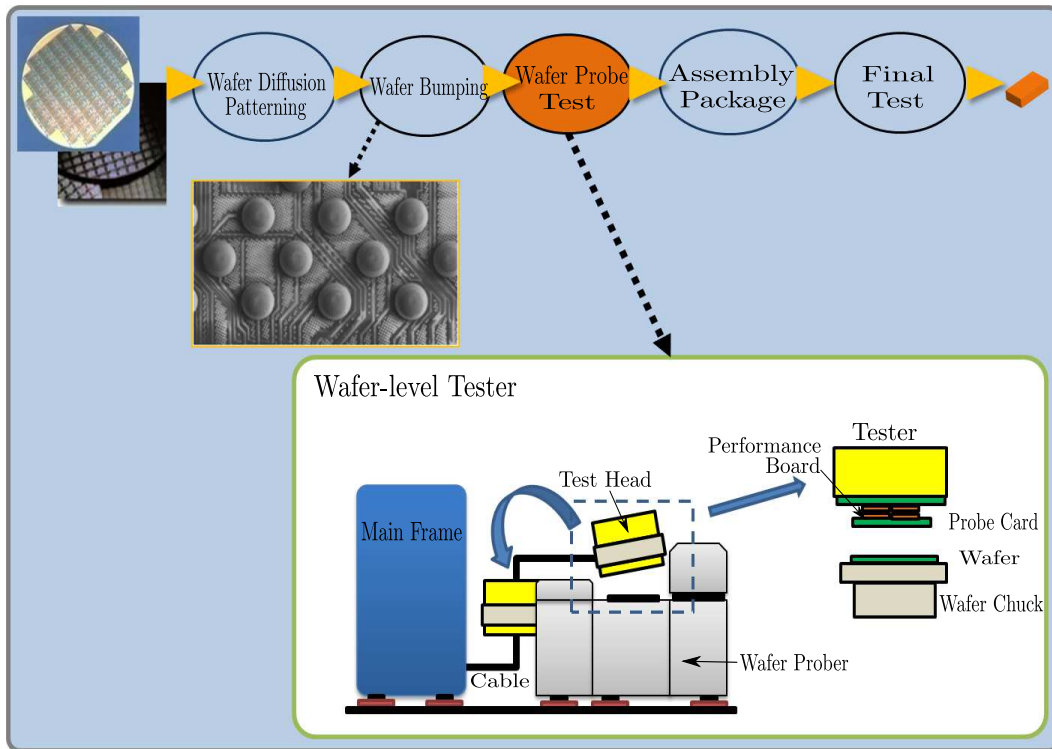


Figure 2.1: Schematic of the wafer-level test

probe cards with modern configurations. In the cantilever probe card, the needles with the lowest vertical alignment scrub the most because the same amount of overdrive is applied to all needles by the probe card to guarantee that all probe tips make contact with the wafer surface. Furthermore, when overdrive is applied to the probe cards, some probe tips fail to contact with the bumps on modern wafers since they are getting smaller than before (see Fig. 2.2). For these reasons, other types of probe cards, vertical and MEMS, were developed to resolve them. Although some vendors like AMD have switched completely to vertical or MEMS cards, cantilever probe cards are still widely used in the wafer test. However, due to many benefits of vertical and MEMS probe cards, the trend of probe cards technology is shifting toward vertical and MEMS design [8]. Table 2.1 shows the

breakdown of types of probe cards that are used for major semiconductor manufacturers.

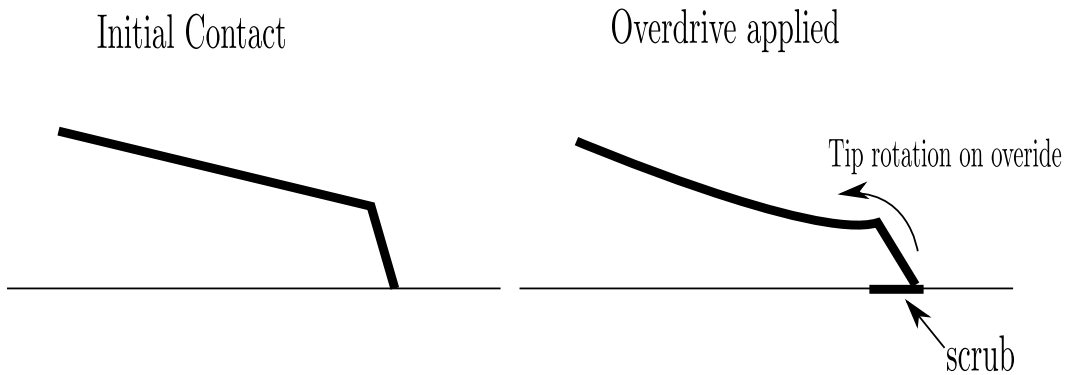


Figure 2.2: Probe with contact pressure applied and resulting scrub [8]

Table 2.1: Probe card technology by manufacturers [8]

Semiconductor manufacturer	Cantilever cards	Vertical or MEMS
Freescall	60%	40%
IBM	51%	49%
Texas Instruments	91%	9%
AMD	0%	100%
Philips	88%	12%
Qimonda	13%	87%

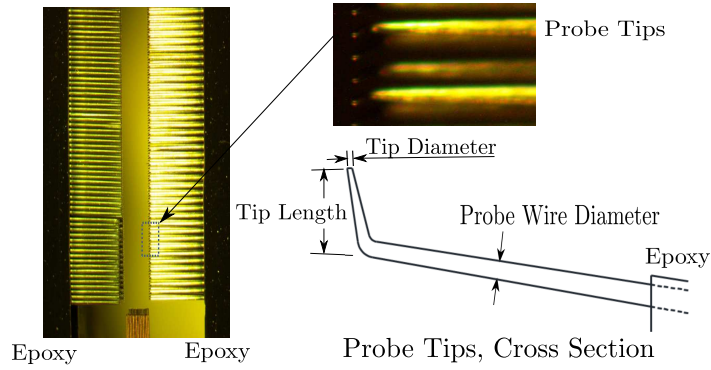
Vertical probe cards are able to correct the long scrub limitation suffered by cantilever probe cards. The vertical probe cards do not completely depend on scrubbing to correct planarization inconsistency; therefore, they reduce scrub length dramatically. Fig. 2.3(b) shows one example of a vertical probe card. In this vertical probe needle design, the vertical probe needle, also called cobra probe tip, is guided by position hole, and establishes electrical contact with bumps on the wafer similar to the cantilever probe needle. This

design apparently resolves problems where needles become relatively misaligned. Moreover, the vertical arrangement provides some advantages that reduce the interference between the needles as well as allow for compact assembly and smaller size. However, despite the advantages, some cobra probe tips can be twisted which may cause electrical short between cobra needles from the buckling of the needles. This risk becomes more prominent with higher density chips, since needles must be assembled with less clearance and are more susceptible to needle-to-needle contact during overdrive.

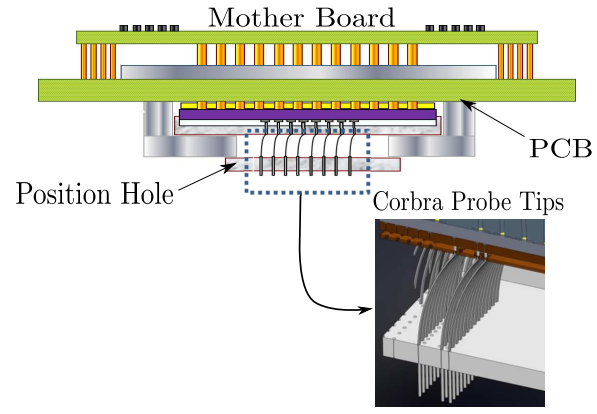
In order to achieve higher density and to resolve the limitation of both cantilever and vertical probe cards, micro-electro-mechanical systems(MEMS)-based probe cards have been developed. They allow for higher probe densities than previous techniques, but at a higher cost. An example of a MEMS probe card is shown in Fig. 2.3(c).

2.1.3 Probe Card Analyzer

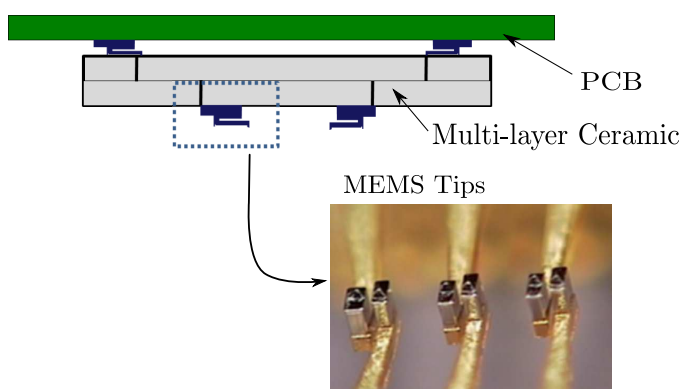
A probe card analyzer is used to detect potential failures in probe cards. A typical probe card analyzer measures positional accuracy, planarity, tip diameter, and scrub length as well as evaluate the tip damage. The measurement values are collected on a per-contact basis, which can be assembled to higher level for evaluating rotational misalignment or regional failures. These measurement results can be used to evaluate a probe card for use in manufacturing flow, or to analyze problems with a probe card. The expected resolution of the problems are probe realignment, probe replacement, probe tip cleaning, planarity adjustment, and chuck adjustment[8]. In the past, manual inspection was used to determine the failures of the probe card, but with the advancement in digital image technologies, most of the commercial probe card analyzers employ imaging systems as the primary means of information gathering. Since most imaging systems of the commercial probe analyzer use



(a) Cantilever type



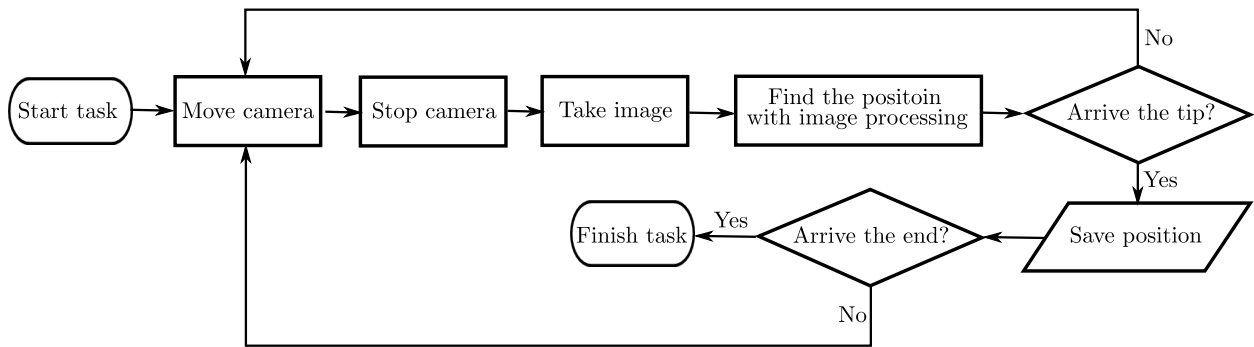
(b) Vertical type



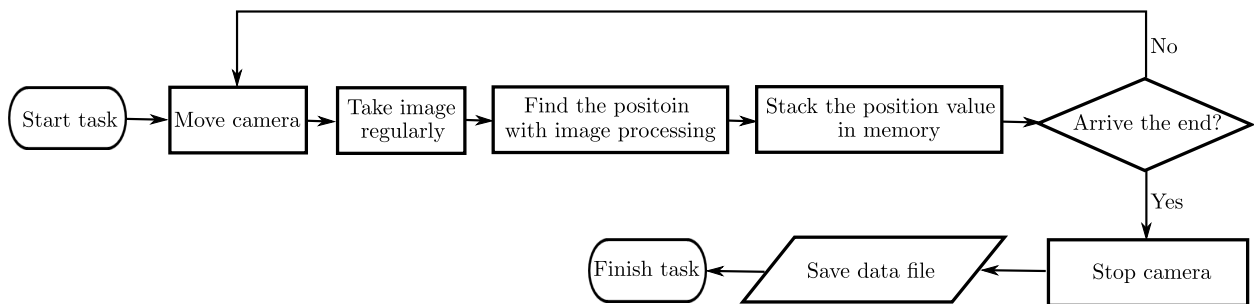
(c) MEMS type

Figure 2.3: Vertical and MEMS type of probe card. (SDA Technology Co., Ltd.)

conventional stop-and-go method for capturing and processing the image (see Fig. 2.4(a)), probe card analyzers spend tremendous time at the stop-and-go stage. In this paper, an on-the-fly method which simultaneously performs the measurement tasks while the camera is in motion is proposed(see Fig. 2.4(b)).



(a) Conventional stop-and-go algorithm



(b) Proposed on-the-fly algorithm

Figure 2.4: Image acquisition algorithm

2.2 Real-time Coordination of Vision and Motion Data

This section briefly defines real-time system and reviews latency that is one of the main technical issues for the new probe card analysis.

2.2.1 Real-time System

In order to achieve faster measurement for the proposed probe card analysis, the new vision-based probe card analyzer captures and processes the vision image while the camera is in motion, and the entire inspection tasks are completed in real-time. A real-time system must fulfill explicit bounded response-time constraint to prevent failure[19]. In the others words, a real-time system timely provide the task results when they are needed [41]. Timeliness of a vision system can be expressed as a value function. In a conventional machine vision application where the camera or the object stops for taking the image and is not moved until the vision system has made its decision, there is some value to the vision system making a decision by a certain time so that it is not the slowest part of the measurement tasks. If the vision system is faster than this time, its value is not increased because the moving stage cannot go any faster. If the vision system is always on time, but frequently a bit slower, its value might be reduced only slightly. However, as the vision system becomes slower on average or more frequently, it becomes a bottleneck, and its value declines eventually becoming negative. The system that misses the deadlines which leads to performance degradation but not failure would be called soft real-time. In the proposed measurement system, the value function is high only when the measurement task is completed before starting the next task. If the vision system is either too fast or too late, its value is negative. The system that must meet the deadline which leads to total system failure would be called hard real-time [41].

Technically, the time between an event and a response to that event is called latency. In a real-time system the latency will be deterministic; the response will happen at an expected time after the event. The latency of the proposed system will be dealt with next section.

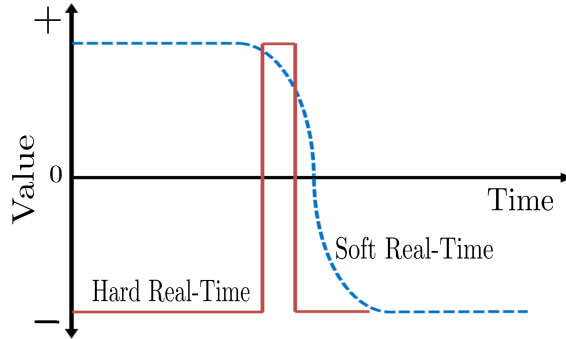


Figure 2.5: Value function for soft and hard real-time [41]

2.2.2 Latency

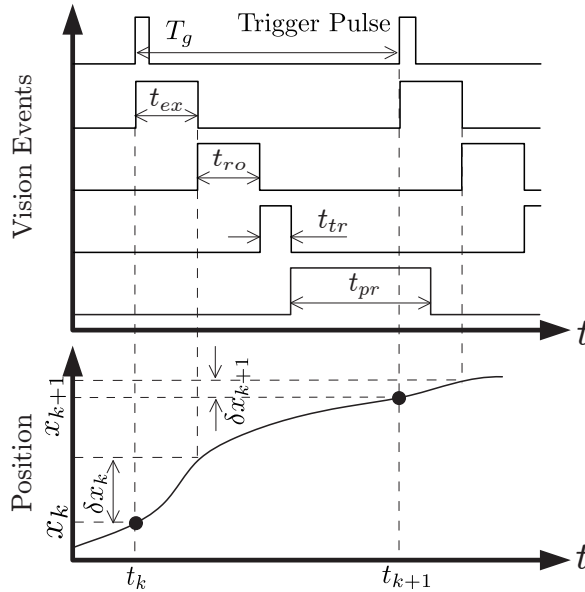


Figure 2.6: Timing diagrams of vision events and the object position

To use camera images as reference data, we firstly need to keep track of the exact moment when each image is taken. This can be achieved by real-time triggering and compensation of latency. The latency of a vision system mainly comes from the exposure time

t_{ex} (accumulating light into electrical charges), the readout time t_{ro} (converting charges into digital data), the transfer time t_{tr} (transferring data into the processor) and the processing time t_{pr} . The total latency T_L is thus given by

$$T_L = t_{ex} + t_{ro} + t_{tr} + t_{pr} + \delta t. \quad (2.1)$$

where δt stands for the jitter, i.e. the uncertainty in the latency. The amount of jitter should be minimized in applications requiring high determinism. Figure 2.6 shows the timing diagram of a vision system synchronized with the measured position (x) of the target object. Using carefully configured triggering operation and proper machine vision protocols (e.g. the Camera Link or the GigE vision), t_{ex} , t_{ro} , and t_{tr} (which constitute the hardware latency) can be kept almost constant. On the other hand, the software latency due to the processing time t_{pr} , typically varies with each image sample. Let us denote the maximum and the minimum values for t_{pr} by \bar{t}_{pr} and \underline{t}_{pr} , respectively, (i.e. $\underline{t}_{pr} \leq t_{pr} \leq \bar{t}_{pr}$). As shown in Fig. 2.6, the image processing starts right after the completion of the transmission. As long as the completion of image processing (i.e. the falling edge of t_{pr} pulse) occurs before the transmission of the next image data (i.e. the falling edge of the next t_{tr} pulse), image processing does not cause any backlog. In other words, two consecutive t_{pr} pulses do not overlap in the timing diagram of Fig. 2.6. Therefore, the period of the trigger pulse denoted by T_g ($= t_{k+1} - t_k$) must be chosen as follows to guarantee the real-time image processing:

$$T_g \geq \max(\bar{t}_{pr}, t_{ex} + t_{ro} + t_{tr}). \quad (2.2)$$

If we send a trigger pulse at $t = t_k$, the electronic shutter immediately starts to integrate the image data. Any information drawn from this image will be available at $t = t_k + T_L$. Thus, by knowing the latency and the exact time of trigger, we can synchronize the vision image with the motion data from the stage. On the other hand, movement of the camera

during the exposure time (t_{ex}) will cause motion blurring. Denoting the stage position at time $t = t_k$ by x_k , the motion blurring occurs for the period of $t_k \leq t \leq t_k + t_{ex}$, which corresponds to the displacement δx_k as illustrated in Fig. 2.6.

2.3 Restoration of Image Blurred by Linear Motion

2.3.1 Introduction

Image information is useful in producing measurement references. However, due to imperfections in the imaging and capturing process, the recorded images always include degraded factors of the original scene. Many factors cause image degradation which includes out-of-focus, motion blur, atmospheric turbulence blur, and image processing noise. Image degradation function is a form of bandwidth reduction of an ideal image due to the imperfection image formation process. Relative motion between the camera and the original scene or an optical system that is out of focus will mostly cause the image degradation. When aerial photographs are taken for remote sensing purposes, image degradation factors are introduced by atmospheric turbulence, aberrations in the optics, and relative motion between the camera and the ground. Particularly, the motion-blur can be clearly seen in the images that were captured with long exposure times and the images of fast moving objects. Since the proposed inspection method uses long exposure times and takes images of fast moving objects, the measurement reference images suffer from very strong motion blurs. Image restoration, sometimes referred to as image deconvolution, deals with the reconstruction or estimation of the ideal image from a blurred image. Basically, image restoration attempts to employ an operation on the image that is the inverse of the imperfections in the image acquisition system. In the linear spatially invariant image restoration,

the characteristics of the degradation function and the noise are assumed to be known a priori [4].

In this chapter, we will concentrate on basic methods for removing motion blur from recorded measurement reference. In other words, we assume that other image degradation factors like aberrations in the optics and atmospheric turbulence is ignorable and the additional image noise is constant. The process of image restoration from motion blur comprises two parts: the estimation of the degradation function, and applying a restoration algorithm. This chapter will introduce the motion blur model and some basic algorithms of the image restoration.

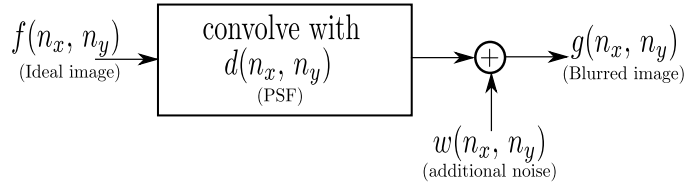
2.3.2 Image formation

In our application, the motion blur is the result of relative motion between the camera and the probe tips during camera exposure. From a mathematical point of view, the blurred image can be considered as a convolution of the ideal image with the blur function. In doing so, we assume that the blurring function acts as a convolution kernel $d(n_x, n_y)$ that does not spatially and mean and correlation function of the image and noise do not spatially. The restoration process can be implemented by means of a linear filter under these conditions. These modeling assumptions can be mathematically represented as follow [4] :

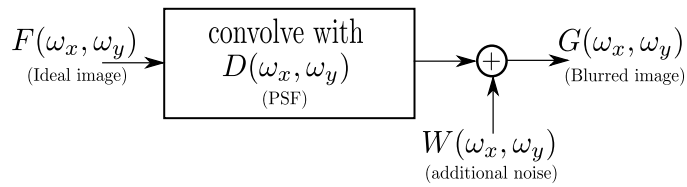
$$\begin{aligned}
 g(n_x, n_y) &= d(n_x, n_y) \star f(n_x, n_y) + w(n_x, n_y) \\
 &= \sum_{i=0}^{M-1} \sum_{j=0}^{N-1} d(i, j) f(n_x - i, n_y - j) + w(n_x, n_y)
 \end{aligned} \tag{2.3}$$

where $g(n_x, n_y)$ and $f(n_x, n_y)$ denote the blurred image and the ideal image, respectively, for each pixel at (n_x, n_y) . M and N are the pixel numbers for x (horizontal) and y (vertical)

directions on the image plane, respectively. $d(n_x, n_y)$ is called the point spread function (PSF) which represents the convolution kernel that describes the blurring mechanism. $w(n_x, n_y)$ is any additional noise affecting the captured image, e.g. electrical noise of image sensors, illumination noise, etc(see Fig. 2.7(a)). If we have a prior knowledge on how the image is blurred, then we can operate the deblurring (or the image deconvolution) by inversely applying $d(n_x, n_y)$ to $g(n_x, n_y)$, the process of which is known as the non-blind image restoration [26]. The specific condition of measuring the probe tips meets the non-blind image restoration because the blurring occurs due to the movement of the x - y stage. The PSF $d(n_x, n_y)$ can thus be described by the stage motion. If we assume the stage is running at a constant speed, the blurring distance δx_k in Fig. 2.6 becomes independent of time, i.e. $\delta x_k = \delta x$ for all $k = 0, 1, \dots$. In this case, the relative motion between the camera and the probe tips is linear and $d(n_x, n_y)$ becomes spatially shift-invariant, i.e. $d(n_x, n_y) = d(n_x - k, n_y - k)$ for all $k = 0, 1, \dots$.



(a) the spatial domain model



(b) the Fourier domain model

Figure 2.7: Image formation model [4]

2.3.3 Linear motion blur

The blurred image is considered as the convolution of an ideal image with 2-D point-spread function (PSF) $d(n_x, n_y)$. The Eq. 2.3 can be interpreted that if the ideal image $f(n_x, n_y)$ would consist of a point source, this point would be captured as a spread-out intensity pattern $d(n_x, n_y)$ thus, the name is called point-spread function.

Most blurring of images is a spatially continuous processes. However, the blur models in continuous forms can be followed by discrete model because identification and restoration algorithms are always based on spatially discrete images. To minimize the errors involved in converting to discrete model, we assume that the sampling rate of the images is high.

The spatially continuous PSF $d(n_x, n_y)$ meets the following three constraints[4]:

- non-negative values only are taken for $d(n_x, n_y)$, due to the physics of the fundamental image formation process
- the PSF $d(n_x, n_y)$ is real-valued, when considering real-valued image
- the imperfections in the image formation process are represented as passive operations, for example no "energy" is absorbed or generated. As a result, the spatially continuous PSF $d(n_x, n_y)$ is constrained to satisfy

$$\int_{-\infty}^{\infty} \int_{-\infty}^{\infty} d(n_x, n_y) dx dy = 1 \quad (2.4)$$

And for spatially discrete blur model:

$$\sum_{i=0}^{M-1} \sum_{j=0}^{N-1} d(i, j) = 1 \quad (2.5)$$

In our model, we assume that the vertical axis of the image plane is aligned with the y coordinate of the stage and that the stage moves along y axis with a constant speed v $\mu\text{m}/\text{sec}$. Then it becomes linear motion blur with the length of motion $\delta x = vt_{ex}$. Denoting the spatial resolution of image sensor along the y axis as s pixels/ μm , the PSF can be given by the moving average filter

$$d(n_x, n_y) = \begin{cases} \frac{1}{L} & \text{if } n_x = 0, 0 \leq n_y \leq L - 1 \\ 0 & \text{otherwise} \end{cases} \quad (2.6)$$

where $L = \lfloor vt_{ex}s \rfloor$ denotes, in the number of pixels, the length of motion during exposure.

By applying the discrete-time Fourier transform to Eq. (2.3) and denoting the transformed signals by capital letters, we get (see also Fig. 2.7(b)):

$$G(\omega_x, \omega_y) = D(\omega_x, \omega_y)F(\omega_x, \omega_y) + W(\omega_x, \omega_y) \quad (2.7)$$

for the spatial frequency (ω_x, ω_y) , where the moving average filter is written as

$$D(\omega_x, \omega_y) = \frac{1}{L} \frac{\sin\left(\frac{\omega_y L}{2}\right)}{\sin\left(\frac{\omega_y}{2}\right)} e^{-j\omega_y\left(\frac{L-1}{2}\right)}. \quad (2.8)$$

Therefore, the image restoration in this case is to find the ideal image $F(\omega_x, \omega_y)$ from the acquired one $G(\omega_x, \omega_y)$ with *a priori* knowledge on $D(\omega_x, \omega_y)$ in the form of Eq. (2.8).

2.3.4 Image Restoration

If we know the PSF $D(\omega_x, \omega_y)$ and the image noise, it may be possible to reconstruct the ideal image. The process of reconstruction of the ideal image from the recorded image that is blurred is called image restoration. Many image restoration techniques has been developed to restore the original image from the blurred image. In this section we will

briefly introduce basic image restoration techniques that are applied in the proposed probe analyzer.

Inverse Filter

Suppose that the point-spread function of the linear restoration filter $h(n_x, n_y)$ has been defined, then the restored image $\hat{f}(n_x, n_y)$ is given by

$$\hat{f}(n_x, n_y) = h(n_x, n_y) \star g(n_x, n_y) \quad (2.9)$$

The simplest approach of the image restoration is the inverse filtering. An inverse filter is a linear filter. The PSF $h_{inv}(n_x, n_y)$ of the inverse filter is the inverse of blurring function $d(n_x, n_y)$ given by

$$h_{inv}(n_x, n_y) \star d(n_x, n_y) = \delta(n_x, n_y) \quad (2.10)$$

The solution of inverse filter in Eq.2.11 seems difficult to design. However, in the spectral domain the solution can be easily found

$$H_{inv}(\omega_x, \omega_y)D(\omega_x, \omega_y) = 1 \implies H_{inv}(\omega_x, \omega_y) = \frac{1}{D(\omega_x, \omega_y)} \quad (2.11)$$

One of the biggest benefits of the inverse filter is that the blur PSF as a priori knowledge is only required, and the inverse filter simply restore the perfect ideal image if noise is absent.

$$\begin{aligned}
\hat{F}_{inv}(\omega_x, \omega_y) &= H_{inv}(\omega_x, \omega_y)G(\omega_x, \omega_y) \\
&= \frac{1}{D(\omega_x, \omega_y)}(D(\omega_x, \omega_y)F(\omega_x, \omega_y) + W(\omega_x, \omega_y)) \\
&= F(\omega_x, \omega_y) + \frac{W(\omega_x, \omega_y)}{D(\omega_x, \omega_y)}
\end{aligned} \tag{2.12}$$

Unfortunately, a small amount of noise is always present in the real world; thus, the second term in Eq. 2.12 does not disappear. In addition, if H_{inv} is a matrix with relatively small values, then the second term in Eq. 2.12 will be very large. In other words, the inverse filtered images cannot be usable because of the excessively amplified noise.

MMSE estimator(Wiener Filter)

The PSF $D(\omega_x, \omega_y)$ is non-minimum phase. Hence, the inverse filtering will amplify the noise $W(\omega_x, \omega_y)$ making it impractical [4]. A more practical way is to formulate the above mentioned deblurring problem as an optimal filter to minimize the mean square error: i.e., given some observation of $g(n_x, n_y)$, say g_1 , find \hat{f} which minimizes the mean squared error (MSE):

$$\min \mathbb{E} \left[|f - \hat{f}|^2 \middle| g = g_1 \right]. \tag{2.13}$$

Note that the blurring model in Eq. (2.7) is a linear system. If we assume that the noise signal $w(\omega_x, \omega_y)$ is zero mean, Gaussian distributed and independent from other signals, the optimal solution to our deblurring problem will be given by the minimum mean square error (MMSE) estimator or Wiener filter:

$$\hat{f}(n_x, n_y) = h(n_x, n_y) \star (g(n_x, n_y) - \bar{g}(n_x, n_y)) + \bar{f}(n_x, n_y). \tag{2.14}$$

$\hat{f}(n_x, n_y)$ denotes the recovered image and the overline ($\bar{\bullet}$) represents the mean value of the corresponding signal. Note that $\bar{f} = \bar{g}$ if w is zero mean. The effect of the mean value

terms in Eq. (2.14) will show up as an offset in the deblurring process and can be adjusted during the calibration. According to the MMSE solution, the Fourier transform of the convolution kernel $h(n_x, n_y)$ is computed as

$$H(\omega_x, \omega_y) = \frac{D^*(\omega_x, \omega_y)}{D^*(\omega_x, \omega_y)D(\omega_x, \omega_y) + K} \quad (2.15)$$

where K is the additive factor given by

$$K = \frac{S_w(\omega_x, \omega_y)}{S_f(\omega_x, \omega_y)}$$

with $S_w(\omega_x, \omega_y)$ and $S_f(\omega_x, \omega_y)$ denoting the power spectrum of the noise w and the ideal image f , respectively. Since both power spectrums are unknown in practice, K is usually treated as a parameter that tunes the effect of sharpening and noise [10].

Chapter 3

Experimental Test Bed

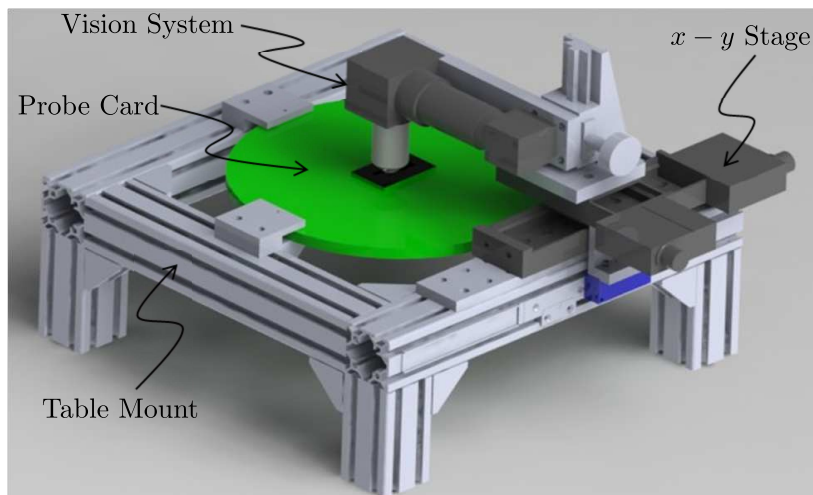


Figure 3.1: Overview of the tabletop probe analysis system used for experiment.

A tabletop probe analyzer has been designed and built to demonstrate the main ideas presented in the previous chapter. The proposed probe analyzer configuration is comprised of two main parts: a micro machine vision system which includes micro optics, an $x-y-z$ stage with a probe card mount, and a real-time controller that communicates with both

the vision camera and the x - y stage indecently so that the motion data and the image data can be synchronized in the way explained in the previous chapter. The micro optics has been designed and embedded into the x - y - z stage that can move x - y axis. Each x - y axis has a micro linear motion stage that consists of a micro lead screw, two linear guide, and a stepping motor. z axis is fixed to the focal length of the lens and does not move during the measurement. A linear encoder is attached beside the y axis to offer the y axis position and velocity of the camera along the y axis. The real-time controller communicates and controls the micro machine vision system with real-time synchronization. The role of the real-time controller is to control the x - y stage, to capture images from the micro optics, and to synchronize both the vision camera and the x - y stage. Fig. 3.1 shows the overview of the proposed micro vision system that is part of the proposed probe analyzer.

3.1 Configuration of the Micro Machine Vision

This section introduces the detailed configuration of the micro machine vision which consists of micro optics, stages and mount. In addition, we briefly introduces the methods of spatial resolution calibration.

3.1.1 Micro optic design

The proposed micro vision system conducts two tasks which are capturing images of the end of probe tips and measuring the positional information of each probe tip. The shape of probe tip seems to be a hook and the diameter of the probe tips is approximately $5\ \mu\text{m}$ $10\ \mu\text{m}$ (see Fig. 2.3(a)). To obtain the position information of the probe tip, it is only need to capture the end of the probe tips. In doing so, objective lens(10x, 20x, or 40x)

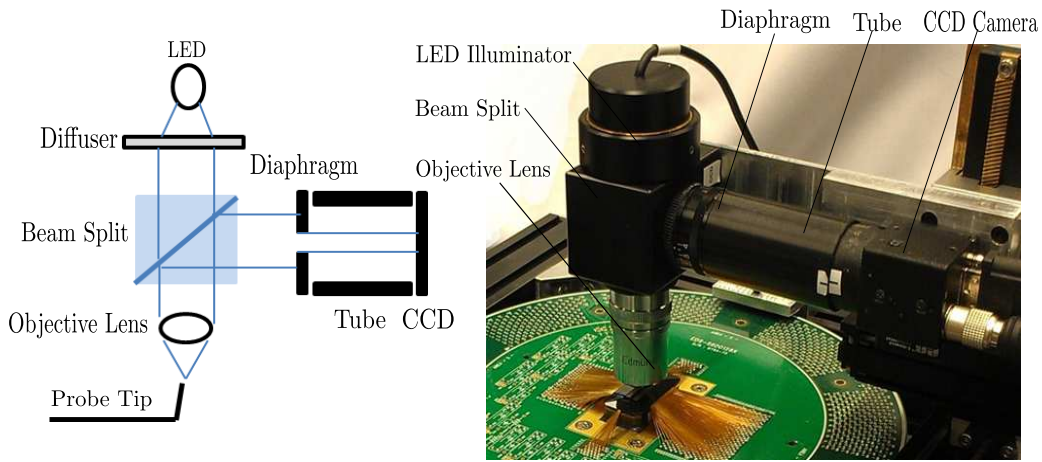


Figure 3.2: Configuration of the machine vision.

are attached to magnify the tiny probe tips and to focus on only a specific spatial point in the air. After evaluating the field of view and the resolution of each objective lens, a 20x objective lens has been selected for the test bed for magnification. Both 10x and 40x image are insufficient to obtain the positional information because 10x image has rough resolution, and the field of view of 40x image is too small to capture the probe tips. In conclusion, the 20x image is adequate in terms of the field of view and the resolution as shown in Fig. 3.3.

Unlike an ordinary microscope, in the probe analyzer, a light source cannot be placed behind the probe card because some probe cards do not have an open window or hole which permits the passage of light. Furthermore, if the light source is located behind the probe card, the machine vision captures the shading image of the probe tips. Therefore, the light source has to be placed onto the top position of the probe card. In addition, the camera is oriented with 90° angle with respect to the LED. The 90° configuration has many advantages in terms of the arrangement because of the compact size. The LED(light-emitting-diode) light source and the diffuser are integrated into the illuminator and a beam

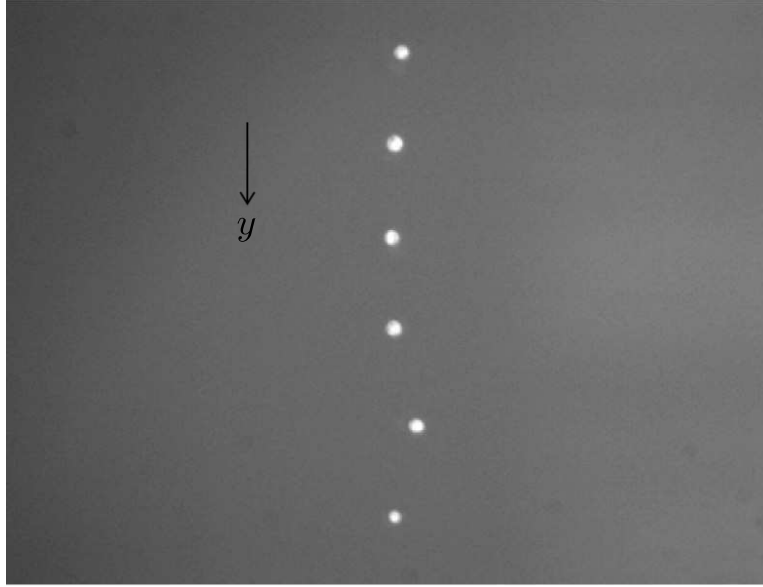


Figure 3.3: A sample still image of pin tips.

split is used to directly project the light onto the probe card and to send the real image to the micro machine vision. A diaphragm adjusts the intensity of the light which controls the brightness of the image. The configuration of the micro machine vision, as shown in Fig. 3.4, is able to directly focus on the specific objects; this, in turn, can capture only the end of the probe tips.

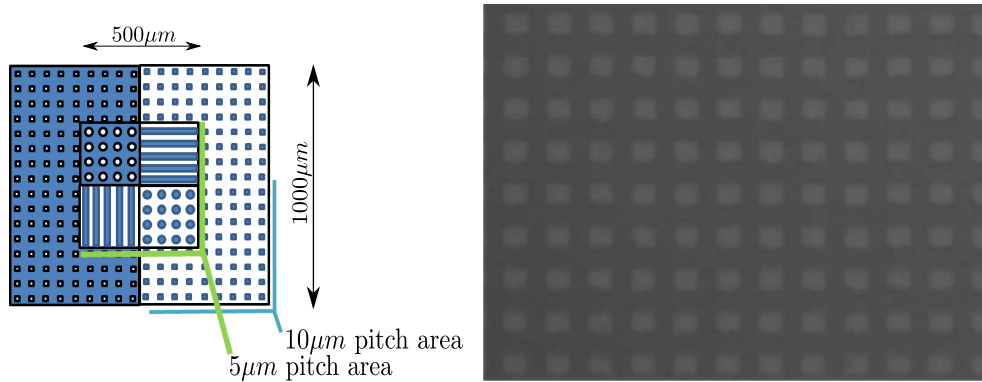
Figure 3.3 shows a sample still image of probe pins with 20x objective lens where the direction of the stage movement (i.e. y direction) is indicated by the arrow. The pin tip has a radius of $5\ \mu\text{m}$ – $10\ \mu\text{m}$ and the pins are located approximately $50\ \mu\text{m}$ apart from each other. The camera model is STC-CL202A manufactured by *Sensor Technologies America, Inc.* Specifications of the camera and its image acquisition system are listed in table 3.1. The exposure time has been chosen to be 10 ms based on the intensity of the light source. The transmission time can be computed using the size of the image data ($=1628 \times 1236 \times 10$

bits) and the speed of the camera link communication protocol (= 255 MB/s).

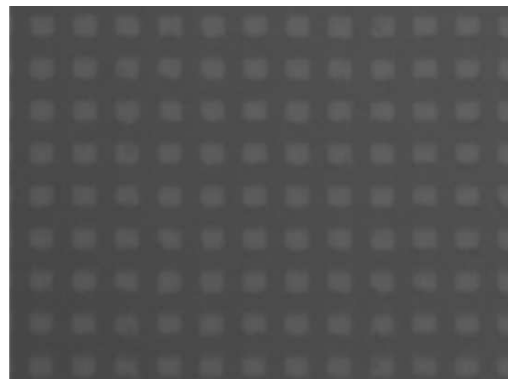
Table 3.1: Specification of the components of the micro machine vision

Components	Specification
CCD Camera	Progressive Scan CCD Communication : Digital Camera Link Resolution: 1628(H)x 1236(V) pixels Bit Depth: 10bit Maximum Frame rate: 15 fps
Objective Lens (10x)	PL L 10/0.25, 160/0
Objective Lens (20x)	DIN 20, 0.40
Objective Lens (40x)	PL L 40/0.60, $\infty/0$
LED Illumination	LED type
Beam Split	C-Mount VIS 50R/50T
Diaphragm	C-Mount IRIS type
Latency	Value
Exposure time (t_{ex})	10 ms
Readout time (t_{ro})	65 ms
Transmission time (t_{tr})	9.87 ms

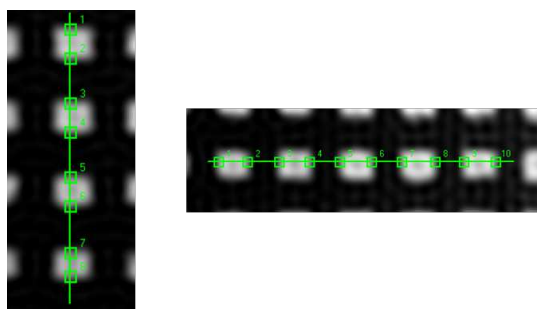
The spatial resolution of the vision image is calibrated using the calibration jig shown in Fig. 3.4(a) which consists of arrays of 5 μm and 10 μm pitch patterns. Using the 10 μm pitch patterns, the vertical pixel resolution of the image data has been calibrated as 40.64 pixels/10 μm which is computed by averaging the distance of eight to ten points as listed in table 3.2.



(a) Calibration Jig



(b) 10 μm pitch pattern



(c) Measure the pattern

Figure 3.4: Spatial Resolution Calibration

Table 3.2: Spatial resolution of the vision image

No. of Tests	Horizontal(pixel/10 μm ,average)	Vertical(pixel/10 μm ,average)
1	40.727	40.830
2	40.564	40.624
3	40.756	40.480
Average	40.682	40.645

3.1.2 Stage and mount

The x - y - z stage consists of a x - y moving axis and a fixed z axis which is adjusted manually. A stacking-type mechanism having two linear stages is utilized into x - y axis. The x - y axis comprises a linear guide, a micro lead screw, a stepping motor, and an embedded controller which is communicated by RS-232 serial communication. Each stage of the x - y axis is driven by a stepping motor, and the movement of y axis is detected by a linear encoder mounted beside the y axis frame. The travel distances of each x - y axis are 50mm and 100mm, respectively. The z axis, a rack and pinion manual stage, is used because the focal length of lens is assumed constant which means the deviation of the focus of the vision camera is ignorable. The x - y - z stage is fixed on the mount. The mount is designed to fix the x - y - z stage, to mount the probe card, and to adjust the height of the probe. The specifications of the x - y - z stage are listed in table 3.3.

3.2 Configuration of Real-time Controller

3.2.1 Configuration

As explained in section 2.2, a deterministic real-time platform that can process the vision data as well as the motion data in time synchrony is needed. For this purpose, the RTOS (realtime operating system) provided by *National Instruments Inc.* is adopted by converting a regular PC into an RT processing machine. The overall configuration of the real-time controller and the associated interface hardware is shown in Fig. 3.5. The real-time controller comprises of a real-time target server and a host server. The host server communicates to the real-time target server by using the Ethernet communication. The role of the host server is to monitor the target, to download the measurement data, and

Table 3.3: Specification of the components of the x - y - z stage

Components	Specification
x -axis	Travel range: 50.8mm
	Microstep(Default resolution): 47.625nm
	Maximum Speed: 7 mm/s
	Repeatability: less 1 μm
y -axis	Travel range: 101.6mm
	Microstep(Default resolution): 47.625nm
	Maximum Speed: 7 mm/s
	Repeatability: less 1 μm
z -axis	Travel range: 50.8mm
	Rack and Pinion(Brass)
Linear Encoder	Travel range: 240mm
	Resolution: 0.5 μm

to upload the new program that is coded to conduct the tasks of the probe analyzer. The real-time target consists of an image frame grabber, a RS-232 interface for stages, and a reconfigurable input/output device. A real-time operating system(RTOS), NI-RTOS, is installed in the real-time target server to perform the real-time measurement.

3.2.2 Connection

The connection between the micro machine vision and the real-time target server is as follows. The micro optics is connected with an image frame grabber, NI PCIe-1427. The image frame grabber sends a real-time trigger to the vision camera, and the on-the-fly

image that includes the motion blurred image is sent to the image grabber. The micro stage is communicated by RS-232, and is connected to the real-time RS-232 interface card, NI PCIe-8432. The linear encoder offers the synchronized movement data to the real-time controller, and a reconfigurable input/output board, NI PCIe-7841R, is used to acquire the movement information. To generate the real-time trigger, image acquisition device and reconfigurable input/output board share the real-time system integration(RTSI) bus by connecting an internal 34-pin connector.

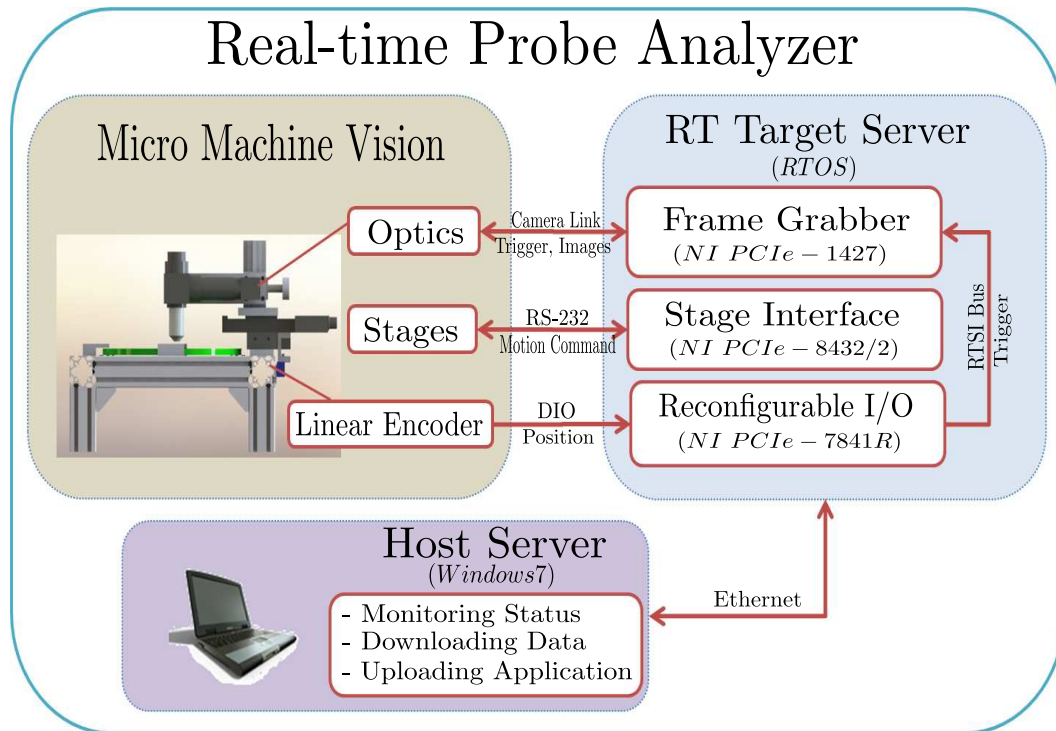


Figure 3.5: Configuration of realtime controller.

Chapter 4

Experimental Results

The new vision-based probe card analyzer is tested to verify the proposed real-time image acquisition algorithm, where deterministic sampling for machine vision and image restoration technique is adopted. In this chapter, we describe the experimental test condition, review the verification results of the image restoration, image combination method, and overall accuracy of the proposed experiment.

4.1 Experimental test condition

The experimental test has been conducted with running the stage at five different speeds: 0.2, 0.4, 0.6, 0.8 and 1.0 mm/s. The trigger period of $T_g = 130$ ms is chosen considering the stage speed and the data size of each image to be processed. Determining the actual size of pixel data for image processing needs some consideration and will be explained in the next paragraph. Figure 4.1 shows the flowchart of each experimental trial. As soon as the stage starts to move, images are captured every trigger period during which the pixel data

get processed with the synchronized encoder signal for computing x and y coordinates as well as the radius of each pin tip. The computed pin information is then stacked up to a predefined array to be provided to the user at the end of the test.

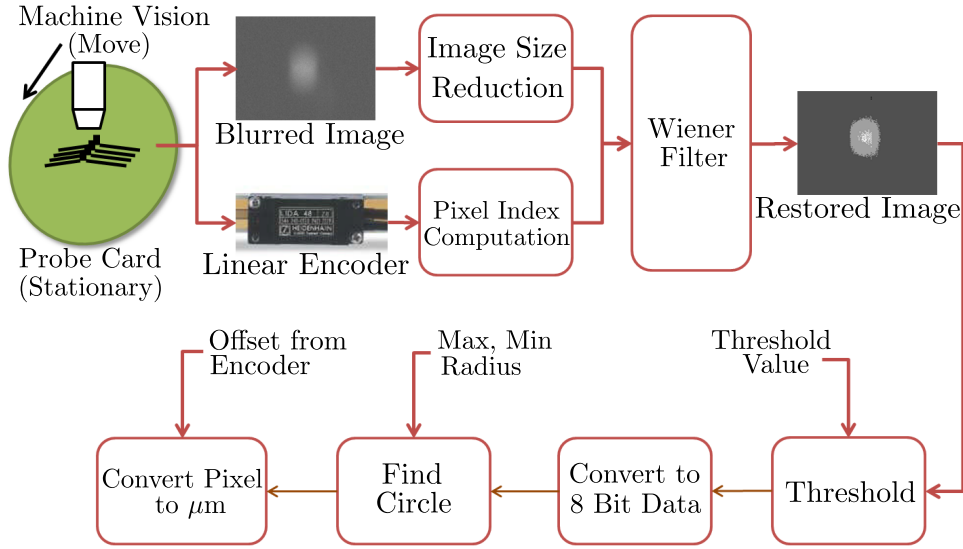


Figure 4.1: Real-time Image Processing Algorithm

As shown in Fig. 4.1, the basic image processing algorithm for the probe tip analysis consists of deblurring (Wiener filtering), thresholding and finding circles to compute their center coordinates and radii. Although these are relatively simple image processing algorithms, the total processing time for 1620×1236 pixel image takes more than 7 seconds in the standard PC, which is not acceptable for our purpose. The simple way to reduce the image processing time is to reduce the size of image data. From Fig. 3.3, we can first note that the pin tips are aligned near the vertical center line and most of the side area is irrelevant to the test. Secondly, for the range of speed we tested (up to 1 mm/s) and the trigger period (130 ms), at least half of the total image data turns out to overlap between two consecutive images. Therefore, we can trim down some pixels along both x

and y directions and, as a result, 255×535 pixels are taken from the original image of 1620×1236 pixel size.

Another point considered in selecting the 255×535 pixel size for online processing is that a small length along y direction actually needs to overlap with the next image. This is because the image of a pin may end up sitting on the boundary with some part of it being clipped. Figure 4.2 shows such a situation where the lower pin of the left-hand side image shows in its entirety while the same pin is clipped in the right-hand side image. As long as the overlap length (denoted by ΔL_y) is large enough to cover the entire length of a pin (including when it is blurred), we can process the pin regardless of clipping.

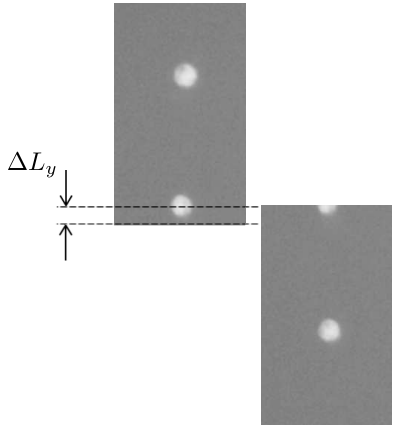


Figure 4.2: Image overlapping for a cropped pin.

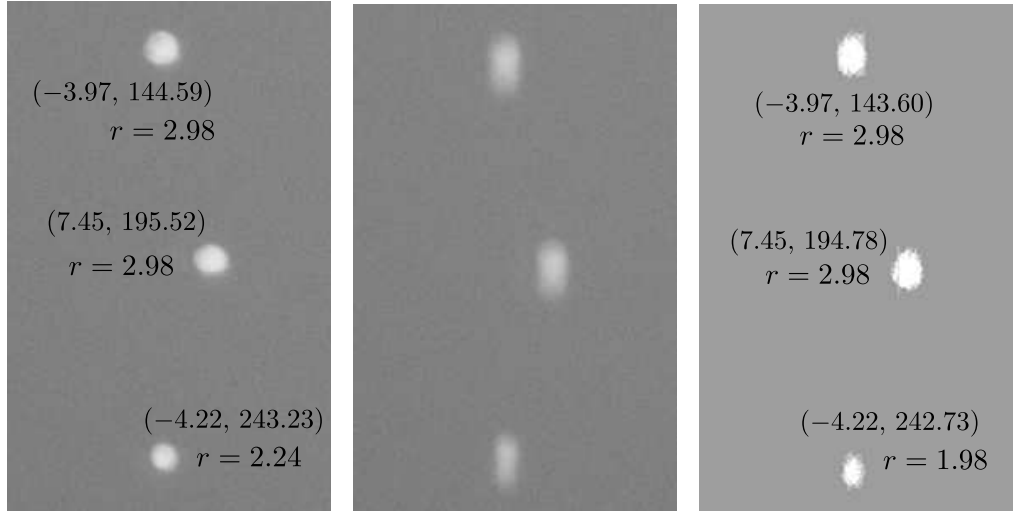
As a result of image reduction explained above, the maximum image processing time \bar{t}_{pr} has been reduced to around 70 ms. Note that the trigger period of our choice $T_g = 130$ ms satisfies Eq. (2.2) since $130 \geq \max(70, 10 + 55 + 9.87) = 84.87$. Table 4.1 summarizes the parameters for experimental results.

Table 4.1: Experimental test conditions.

Parameter	Value
Image size for online processing	255(H) \times 535(V) pixels
Max. processing time \bar{t}_{pr}	61 ms
Camera speed	0.2/ 0.4/ 0.6/ 0.8/ 1 mm/s
Trigger period T_g	390/ 325/ 260/ 195/ 130 ms

4.2 Verification of the image restoration

In order to evaluate the inspection error of the probe card analysis method proposed in this paper, still images are first taken for all probe pins to have their position and radius values computed and spared as reference data. Remember that the pixel resolution is approximately $0.25 \mu\text{m}/\text{pixel}$ as introduced in Section 3.1 and the repeatability of the x - y stage is $1 \mu\text{m}$ at maximum as shown in Table 3.3. Thus, the base error margin of the reference data itself can be considered to be approximately $\pm 1.25 \mu\text{m}$ at maximum. Figure 4.3 compares three different images for the same pins: the still image for reference data (Fig. 4.3(a)), the blurred image captured during the stage motion (Fig. 4.3(b)) and the restored image (4.3(c)). For each pin, the (x, y) coordinates and the radius r are printed in μm scale on Figs. 4.3(a) and 4.3(c) for comparison. For three pins shown here, the x coordinate data from the restored image coincide with those of still image while the y coordinate data and the radius of the bottom pin introduce some errors.



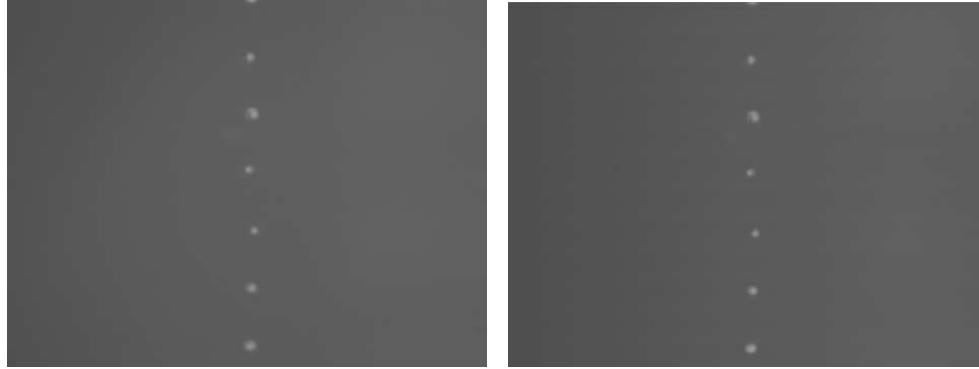
(a) Still image. (b) Blurred image (1 mm/s). (c) Deblurred image

Figure 4.3: Comparison of sample images for three different cases.

4.3 Verification of combined image

Since the overall reference image is a combined image that synthesizes small size images which is acquired at every time period, there is the combined error between the real reference and the combined image. For the verification of the combined image, a reference still image is compared to a combined image(Fig.4.4(b)) that stacks 17 images to reconstruct the reference image. If the position information from the linear encoder is perfectly synchronized, the combined image should be same as the reference still image. Each stacked image is taken at speed 0.2 mm/s and trigger period of $130\mu\text{m}$ to maximize the combined error and to minimize the blurred pixels. The reference still image(Fig. 4.4(a)) is captured at the same position with the combined image.

The comparison between the combined image and the reference still image are listed in table4.2. The circular information of the upper 6 probe tips are compared because of the



(a) Reference still image

(b) combined image when $v = 0.2\text{mm/s}$.

Figure 4.4: Comparison between combined and reference still image

total probe tips of the original image. The deviations of the relative center position and the radius of the probe tips are less than $1 \mu\text{m}$ which is less than the base error margin that explains the previous section. The results shows that the proposed methodology using the combined image algorithm is suitable to be used in the new real-time probe card analyzer.

Table 4.2: Error verification of the combined image[Unit: μm]

Tips	Combined Image			Original Image			Deviation		
	X_c	Y_c	R_c	X_o	Y_o	R_o	ΔX	ΔY	ΔR
1	0	0	2.98	0	0	2.73	0	0	-0.25
2	2.98	47.39	3.47	2.73	47.39	3.23	-0.25	0	-0.25
3	-1.24	94.04	2.48	-1.24	94.04	2.48	0	0	0
4	3.47	144.91	2.73	3.23	145.16	2.48	-0.25	0.25	-0.25
5	0.99	193.05	3.23	1.24	193.03	2.98	0.25	0.25	-0.25
6	-0.5	241.19	3.72	-0.25	241.69	3.23	0.25	0.5	-0.5

4.4 Verification of overall accuracy

Experimental results have been collected from a batch of about 80 pins on the probe card. All the pins are inspected at once for each test speed listed in Table 4.1. The inspection error for each pin is then computed using the reference data a priori obtained from still images. The mean and standard deviation of inspection errors are presented in Fig. 4.5 using bar graphs. Overall, the measurement error for the tip size (i.e. r) shows the smallest standard deviation which is around $0.3 \mu\text{m}$ for all test speeds, which is comparable to the pixel resolution. The position errors came out with larger values of standard deviation than that of r with approximate values around $0.5 \mu\text{m}$ and $0.8 \mu\text{m}$ for x and y coordinates, respectively. As can be expected, the direction that causes linear motion blur, i.e. y , introduces the largest inspection error. Nevertheless, standard deviation is still within the base error margin. Compared to x coordinate and r , the inspection error for y coordinate may also be attributed to the resolution of the encoder which is $0.5 \mu\text{m}$ (See Table 3.3). One interesting aspect of results shown in Fig. 4.5 is that the standard deviation of inspection errors is not necessarily proportional to the test speed. This suggests that the Wiener filtering used for deblurring may perform with similar mean square errors at least for the range of speeds considered in this paper.

To take a more detailed look of performance, the actual distributions of inspection errors are plotted in Fig. 4.6 by normalized histograms for two test speeds: 0.8 mm/s and 1.0 mm/s . We can see the histograms are close to the normal distribution. For the number of pins tested in the experiment, the maximum error for r and x coordinate is around $\pm 1 \mu\text{m}$ while that of y coordinate is around $\pm 1.5 \mu\text{m}$.

To compare the inspection speed, another test algorithm has been created and tested based on the primitive stop-and-go approach. The maximum speed in this case is observed

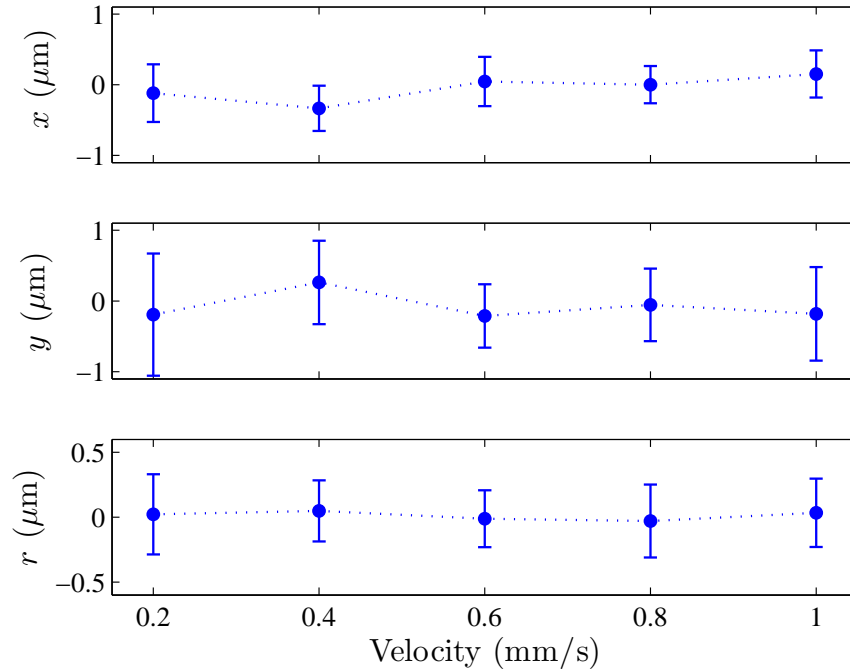
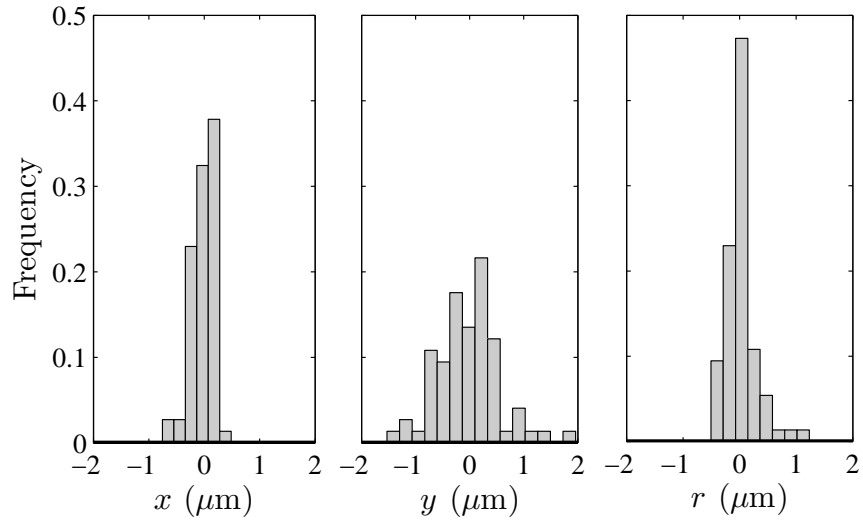
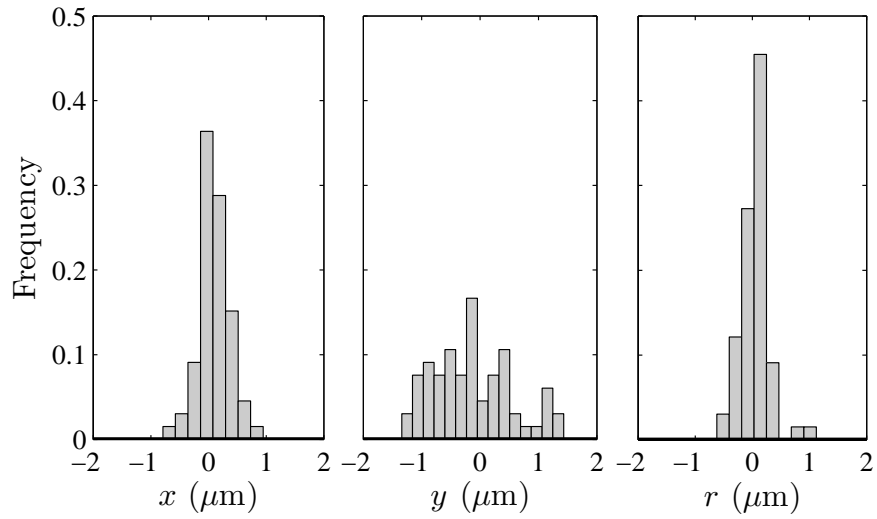


Figure 4.5: Mean and standard deviation of measurement errors of tip position and radius.

to reach 2 pins per second at maximum for the same probe card. From the fact that pins are about $60 \mu\text{m}$ distance apart, we can expect that the proposed probe card analysis technique operated with 1 mm/s of stage speed will result in the inspection speed equivalent to 16.7 pins per second. This corresponds to around $8\times$ improvement compared to the sop-and-go approach.



(a) Histograms for error distributions when $v = 0.8\text{mm/s}$.



(b) Histograms for error distributions when $v = 1.0\text{mm/s}$.

Figure 4.6: Histograms that show error distributions of x , y and r for two different speeds of camera movement.

Chapter 5

Conclusion and Future Work

5.1 Conclusion

A new cost-effective probe card analysis strategy has been proposed to achieve faster inspection in the probe card analyzer. The main idea is to operate the vision-based inspection on-the-fly while the camera is continuously moving. In spite of its simplicity, (non-real-time) latency and image blurring are the big obstacles to implement the proposed simple idea in precision applications. It is also difficult to determine at what location the stage was located while the image is being taken because the vision and the stage may operate asynchronously at different sample rate. In addition, the relative movement during the image capture causes the degradation of reference image for the inspection.

To accomplish these, deterministic sampling for machine vision and simple image restoration technique are adopted. Firstly, the position measurement from the encoder is synchronized with the image data that is captured by a controlled trigger signal under the real-time setting. A consistent latency to coordinate the timing of position data with

that of the vision image is able to be established with some simple calibration of event timings based on stage motion. Secondly, the degradation of the reference image due to the relative motion between the stage and the camera is reconstructed by employing a simple deblurring technique. Since the image degradation function (PSF) of the motion blur is known in this application since the relative motion can be measured, Wiener filter, one of the most popular linear filter based on the minimum mean square error (MMSE), is adopted.

An experimental test bed and a commercial probe card has been designed to demonstrate the main ideas. The experimental test bed comprises a micro machine vision system and a real-time controller. The micro machine vision consists of micro optics and a x - y - z stage with a probe card mount. The main role of real-time controller is to control the x - y stage and capture the image deterministically. The real-time image processing algorithm is employed using NI-labVIEW code.

The ideas of combined image and the deblurring image are verified by comparing them to the reference still image. Lastly, the overall inspection error of the probe card analysis method is evaluated by comparing the reference image from the stop-and-go approach with the image from the proposed on-the-fly approach. As a result of the experimental tests, the inspection speed can be significantly increased compared to the conventional stop-and-go approach with the inspection error still contained within the range of base error margins corresponding to the quantization level of encoder and the pixel resolution.

5.2 Future Work

Although the proposed probe card analyzer achieved the faster inspection with the acceptable inspection error, much effort is still requested to apply to the precision application.

Firstly, precise x - y - z stage and high resolution linear scale are needed to improve overall accuracy and to reduce the base error margin that is approximately $\pm 1.5 \mu\text{m}$. Once we use more accurate micro stage with the precision linear encoder, the base error margin will be more fine-tuned and the overall precision of the system will be also improved. In addition, since the low cost x - y stage use stepping motor, there is a limitation of motion control for the camera motion. If servo-based motion control is applied, we would be able to apply more various control strategies and to achieve better precision. Lastly, in spite of the other degradation due to aberration in the optic is ignorable, the aberration is still existent in the precision system. To deal with uncertainty from the aberration, other deblurring methods that is based on the blind image restoration algorithm [21, 32, 37] will improve the error of the image restoration itself.

References

- [1] N Aleixos, J Blasco, F Navarrón, and E Moltó. Multispectral inspection of citrus in real-time using machine vision and digital signal processors. *Computers and electronics in agriculture*, 33(2):121–137, 2002.
- [2] Mark R Banham and Aggelos K Katsaggelos. Digital image restoration. *Signal Processing Magazine, IEEE*, 14(2):24–41, 1997.
- [3] R Dennis Bates. The search for the universal probe card solution. In *Test Conference, 1997. Proceedings., International*, pages 533–538. IEEE, 1997.
- [4] Alan Conrad Bovik, editor. *Handbook of image and video processing*. Elsevier Academic Press, 2nd edition, 2005.
- [5] Alan Conrad Bovik. *The essential guide to Image Processing*. Academic Press, 2009.
- [6] Hao-Yuan Chang, Wen-Fung Pan, and Shueei-Muh Lin. Experimental and theoretical investigation of needle contact behavior of wafer level probing. *Precision Engineering*, 35(2):294–301, 2011.

- [7] Xiaogang Chen, Xiangjian He, Jie Yang, and Qiang Wu. An effective document image deblurring algorithm. In *Computer Vision and Pattern Recognition (CVPR), 2011 IEEE Conference on*, pages 369–376. IEEE, 2011.
- [8] William Robert Farner. *On-chip probe metrology*. ProQuest, 2008.
- [9] Rafael C Gonzalez, Richard E Woods, and Steven L Eddins. *Digital image processing using MATLAB*, volume 2. Gatesmark Publishing Tennessee, 2009.
- [10] Domenico Grimaldi, Francesco Lamonaca, and Carmelo Macrì. Correction of the motion blur alteration in the human lymphocyte micro-nucleus image based on wieners deconvolution. In *Proc. of 16th IMEKO TC4 Symp*, pages 22–24, 2008.
- [11] Soo Jeon, Masayoshi Tomizuka, and Tetsuaki Katou. Kinematic kalman filter (kkf) for robot end-effector sensing. *Journal of dynamic systems, measurement, and control*, 131(2), 2009.
- [12] Hui Ji and Kang Wang. A two-stage approach to blind spatially-varying motion deblurring. In *Computer Vision and Pattern Recognition (CVPR), 2012 IEEE Conference on*, pages 73–80. IEEE, 2012.
- [13] Xiaoyi Jiang, Da-Chuan Cheng, Steffen Wachenfeld, and Kai Rothaus. Motion deblurring. *University of Muenster, Department of Mathematics and Computer Science*, 2005.
- [14] Neel Joshi, Sing Bing Kang, C Lawrence Zitnick, and Richard Szeliski. Image deblurring using inertial measurement sensors. *ACM Transactions on Graphics (TOG)*, 29(4):30, 2010.

- [15] Aggelos K Katsaggelos. Iterative image restoration algorithms. *Optical engineering*, 28(7):287735–287735, 1989.
- [16] Bong-Hwan Kim and Jong-Bok Kim. Design and fabrication of a highly manufacturable mems probe card for high speed testing. *Journal of micromechanics and microengineering*, 18(7):075031, 2008.
- [17] Bong-Hwan Kim, Jong-Bok Kim, and Jong-Hyun Kim. A highly manufacturable large area array mems probe card using electroplating and flipchip bonding. *Industrial Electronics, IEEE Transactions on*, 56(4):1079–1085, 2009.
- [18] Chang Jin Kim, Ho Jung, Jae Chang Yang, Seong Ho Kong, Dong Sue Jang, and Cheol Kim. Fabrication of a mems-based fine-pitch cantilever-type probe unit. In *Sensors, 2006. 5th IEEE Conference on*, pages 530–533. IEEE, 2006.
- [19] P.A. Laplante and A.D. Stoyenko. *Real-time imaging: theory, techniques, and applications*. Electrical engineering.
- [20] Brian Leslie and Farid Matta. Membrane probe card technology (the future for higher performance wafer test). In *Test Conference, 1988. Proceedings. New Frontiers in Testing, International*, pages 601–607. IEEE, 1988.
- [21] Anat Levin, Yair Weiss, Fredo Durand, and William T Freeman. Understanding and evaluating blind deconvolution algorithms. In *Computer Vision and Pattern Recognition, 2009. CVPR 2009. IEEE Conference on*, pages 1964–1971. IEEE, 2009.
- [22] De-Shin Liu, Chi-Min Chang, Chin-Yi Tu, An-Hong Liu, Cheng-Fang Huang, and Yi-Chang Lee. Optimization of multilayer probe card using strain energy-based analytical model and multiobjective programming algorithm. *Components, Packaging and Manufacturing Technology, IEEE Transactions on*, 1(8):1292–1302, 2011.

- [23] William R Mann, Frederick L Taber, Philip W Seitzer, and Jerry J Broz. The leading edge of production wafer probe test technology. In *Test Conference, 2004. Proceedings. ITC 2004. International*, pages 1168–1195. IEEE, 2004.
- [24] Rob Marcelis. H3d profiler for contact less probe-card inspection. In *IEEE Southwest Test Workshop*. IEEE, June 2012.
- [25] James G Nagy and Dianne P O’Leary. Restoring images degraded by spatially variant blur. *SIAM Journal on Scientific Computing*, 19(4):1063–1082, 1998.
- [26] SK Nayar and M Ben-Ezra. Motion-based motion deblurring. *IEEE Transactions on Pattern Analysis and Machine Intelligence*, 26(6):689–698, 2004.
- [27] Greg Olmstead and Bob Davis. Testing probe cards that contain complex circuitry. *Solid State Technology*, 55(7):20–23, 2012.
- [28] Seiji Sasho and Teruhisa Sakata. Four multi probing test for 16 bit dac with vertical contact probe card. In *Test Conference, 1996. Proceedings., International*, pages 86–91. IEEE, 1996.
- [29] Rod Schwartz. Measurement repeatability key to probe-card metrology. *EE Evaluation Engineering*, 37(9), 1998.
- [30] George Seward. Optical design of microscopes. SPIE, 2010.
- [31] Radovan Stojanovic, Panagiotis Mitropulos, Christos Koulamas, Yorgos Karayiannis, Stavros Koubias, and George Papadopoulos. Real-time vision-based system for textile fabric inspection. *Real-Time Imaging*, 7(6):507–518, 2001.

- [32] Murali Subbarao, Youn-sik Kang, Satyaki Dutta, and Xue Tu. Localized and computationally efficient approach to shift-variant image deblurring. In *Image Processing, 2008. ICIP 2008. 15th IEEE International Conference on*, pages 657–660. IEEE, 2008.
- [33] Murali Subbarao, T-C Wei, and Gopal Surya. Focused image recovery from two defocused images recorded with different camera settings. *Image Processing, IEEE Transactions on*, 4(12):1613–1628, 1995.
- [34] T Tada, R Takagi, S Nakao, M Hyozo, T Arakawa, K Sawada, and M Ueda. A fine pitch probe technology for vlsi wafer testing. In *Test Conference, 1990. Proceedings., International*, pages 900–906. IEEE, 1990.
- [35] Tao Tao. *Multispectral Method for Apple Defect Detection using Hyperspectral Imaging System*. PhD thesis, 2011.
- [36] Yaqin Tao, Huosheng Hu, and Huiyu Zhou. Integration of vision and inertial sensors for 3d arm motion tracking in home-based rehabilitation. *The International Journal of Robotics Research*, 26(6):607–624, 2007.
- [37] Xue Tu, Murali Subbarao, and Youn-Sik Kang. A new approach to 3d shape recovery of local planar surface patches from shift-variant blurred images. In *Pattern Recognition, 2008. ICPR 2008. 19th International Conference on*, pages 1–5. IEEE, 2008.
- [38] Fei Wang, Rong Cheng, and Xinxin Li. MemS vertical probe cards with ultra densely arrayed metal probes for wafer-level ic testing. *Microelectromechanical Systems, Journal of*, 18(4):933–941, 2009.
- [39] Otto Weeden. Probe card tutorial. *Keithley Instruments, Inc*, pages 1–40, 2003.

- [40] Perry C West. Machine vision in practice. *Industry Applications, IEEE Transactions on*, (5):794–801, 1983.
- [41] Perry C West. High speed, real-time machine vision. *Imagination and Automated Vision Systems, Inc*, 2001.
- [42] Kim-Hui Yap, Ling Guan, Stuart William Perry, and Hau San Wong. *Adaptive image processing: a computational intelligence perspective*. Crc Press, 2010.